Available online at www.sciencedirect.com
ScienceDirect
Trans. Nonferrous Met. Soc. China 33(2023) 1550−1558
Transactions of Nonferrous Metals Society of China
www.tnmsc.cn

Application of aeromagnetic survey to mineral exploration of Jinping, Yunnan, China by using multirotor UAV

Jian-xin LIU[1,2], Hui-peng LIU[1,3], Rong LIU[1,2], Jian-qiang XUE[1,2], Yue-hua LI[4], Fang WANG[3]

1. School of Geosciences and Info-Physics, Central South University, Changsha 410083, China;
2. Hunan Key Laboratory of Nonferrous Resources and Geological Hazard Detection, Central South University, Changsha 410083, China;
3. Yunnan Key Laboratory of Geotechnical Engineering and Geohazards, Kunming Prospecting Design Institute of China Nonferrous Metal Industry Co., Ltd., Kunming 650051, China;
4. Climate Change Research Center, University of New South Wales, Sydney NSW 2052, Australia

Received 25 November 2021; accepted 7 April 2022

Abstract: Jingping, Yunnan, China, is an unfriendly area for ground survey due to the high altitude, rough terrain and dense vegetation. To detect the concealed magnetite ore bodies in this area, the aeromagnetic survey in a 7.8 km^2 region was carried out. The field experiments were conducted to investigate the source and level of the noise. Then, the proton magnetometer was placed 3 m under the multirotor unmanned aerial vehicle (UAV) to decrease the static interference. The inverse distance weighting interpolation algorithm with a nonlinear filter was proposed to suppress the noise and dynamic interference caused by the strong wind. The results show that these methods can alleviate the interference of the UAV rotor and strong wind effectively. The patterns of the data from our aeromagnetic survey agree well with the horizontal distribution of the magnetic strata deduced from the geological background. Furthermore, the concealed mafic magmatic rocks and the titanium magnetite inferred from the aeromagnetic survey are confirmed by 4 drill logs in the study area, which supports the validity of the UAV aeromagnetic survey.

Key words: aeromagnetic survey; multirotor UAV; noise suppression; concealed titanium magnetite

1 Introduction

The aeromagnetic method uses an aircraft carrying the magnetometer to investigate the area that is hard for ground survey. Its high sampling rate of the geomagnetic field in a large survey area is welcomed and boosts efficiency for the fieldwork. The potential use of the aeromagnetic method in geological research has attracted much attention, such as small-scale geological mapping and surveying large-scale geological structures [1−3].

In mineral exploration, the aeromagnetic survey is usually carried out in the early exploration stage to analyze the geological conditions and locate the concealed ore body [4,5]. As the simplest airborne geophysical method, aeromagnetic work can be completed with a magnetometer hoisted by a small fixed-wing unmanned aerial vehicle (UAV) [6,7]. However, high-speed fixed-wing UAV has safety concerns for low-height flight in mountainous area. Magnetometers can be mounted to helicopters for aeromagnetic surveys [8,9]. Nevertheless, the expensive cost and safety concerns of helicopter operation are obstacles to applying the aeromagnetic method. The airships are also options for aeromagnetic work [10], but they are highly susceptible to wind and difficult to control.

Multirotor UAV, with the advantages of flexibility, low cost, and easy-to-control, is quite

Corresponding author: Rong LIU, E-mail: liurongkaoyan@126.com
DOI: 10.1016/S1003-6326(23)66202-8

suitable for near-surface magnetic surveys. There are successful aeromagnetic surveys that have been conducted using multirotor UAV equipped with Overhauser magnetometer [11], three-axis fluxgate magnetometers [12,13], and optical pump magnetometers [14,15]. The three-axis fluxgate magnetometer is light in mass, while its accuracy is nearly two orders different from that of the proton magnetometer. As the most cost-effective magnetometer currently, the proton magnetometer is widely used by various exploration groups [16,17].

The compensation calculation is the common technique to recover the magnetic interference during aeromagnetic survey by the multirotor UAV [18,19]. The UAV has multiple motors, and the dynamic electromagnetic interference resulted by the speed difference between those motors should be denoised. Typically, static magnetic interference of the UAV in stable state decreases rapidly with the increase of distance from the magnetometer, and it can be removed by placing the magnetometer under the multirotor UAV with enough distance. However, the dynamic interference of multirotor UAV caused by external force such as strong wind will bring about strong random noise due to the large speed difference between different motors. Therefore, it is necessary to study the noise reduction of the magnetic interference, especially the dynamic interference of UAV during the aeromagnetic survey.

The geological data from Jinping, Yunan, China, suggest that this area has concealed ore bodies due to a continuous intensification of crustal movement. However, a ground magnetic survey in the target region is not available because of the high altitude and rough terrain. In this work, the proton magnetometer mounted on a multimotor UAV was adopted to carry out the aeromagnetic survey, yielding a 156 km flight line covering 7.8 km^2. Before the survey, both the static interference of the drone and the dynamic interference by gusts at high altitudes were evaluated based on field experiments. Subsequently, we proposed an appropriate separation between the UAV and magnetometer for the fieldwork and a nonlinear filter to correct the measured data. These suppressed the static interference to the drone within an acceptable level and eliminate the local negative anomalies from the dynamic interference during the strong wind. Finally, it is demonstrated that the results of the aeromagnetic survey agree well with the geological background data, and the following drills verify the titanium magnetite deposit inferred from the aeromagnetic survey.

2 Geological background

We carried out the geological mapping work of the study area before the aeromagnetic survey in 2020. Figure 1 shows that the main exposed strata in this area is Fenggang formation (Pt_1f) of Proterozoic Ailaoshan group. The main lithology of Fenggang formation of Ailaoshan group is amphibolite plagioclase gneiss, biotite amphibolite plagioclase gneiss, amphibolite, plagioclase gneiss and felsic migmatite. The Fenggang formation exposed in this area has thickness greater than 1330 m, which is in contact with acid intrusive rock ($\gamma_5^{1(a)}$) in the southwest.

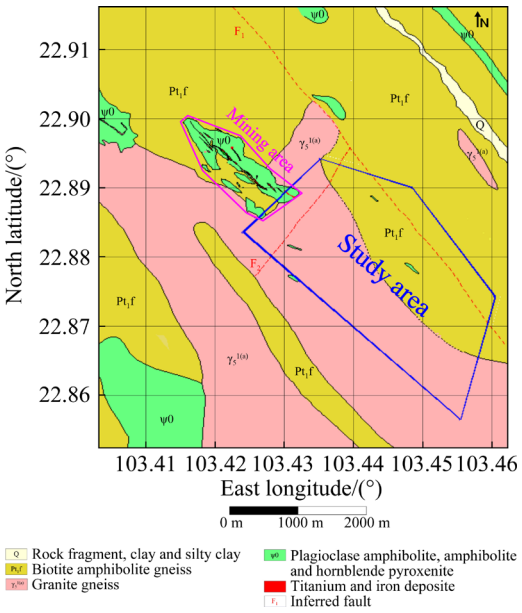

Fig. 1 Geological map of study area

Mesozoic acid intrusive rock is widely distributed in this area. Its lithology is mainly granite gneiss, light gray and gray white, with granular crystalloblastic structure. The rock is mainly composed of plagioclase and quartz, followed by biotite, amphibole, clinopyroxene, chlorite and epidote. The acid intrusive rock has no direct genetic relationship with iron ore deposits.

The basic magmatic rock (ψ0) which intruded into Fenggang formation and acidic magmatic rocks in the late Mesozoic has a direct genetic

relationship with the formation of ilmenite ore body. The basic magmatic rocks in the mining area are distributed along the NW−SE direction, and titanomagnetite is contained in the basic magmatic rocks. As shown in Fig. 2, NW−SE trending faults provide a channel for the intrusion of basic magma. A small part of basic magmatic rocks are exposed to the surface, while most of them are hidden underground. Basic magmatic rock is the parent rock of ilmenite. Rock types mainly include amphibolite and amphibolite pyroxenite. The basic magmatic rock is subjected to strong regional metamorphism, and its original mineral composition, structure and structural characteristics have disappeared. The basic magmatic rock is characterized by flake, gneissic and massive structure, which has the same schistosity direction with the surrounding rock.

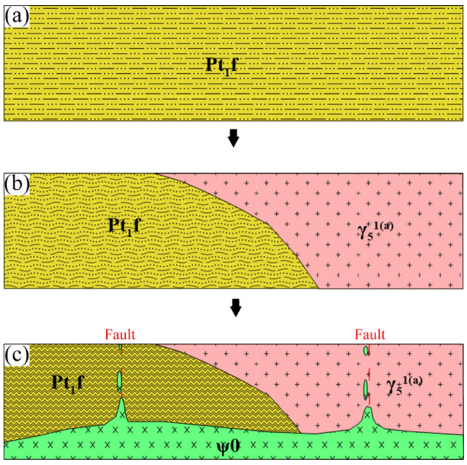

Fig. 2 Stratigraphic evolution diagram

The basic magmatic rocks containing titanomagnetite are distributed along the NW−SE direction. The study area is located in the southeast extension of the basic magmatic rocks in the mining area (see Fig. 1), and there are probably concealed basic magmatic rocks connected with the mining area in the deep. Basic magmatic rocks contain a large number of magnetic minerals, and their magnetism is much higher than that of surrounding rocks. This provides favorable conditions for aeromagnetic survey to explore titanomagnetite related to concealed basic magmatic rocks.

3 Method

3.1 Noise investigation

The UAV used in this project is a DJI Matrice 600 Pro. It is a six-rotor drone with a maximum payload of 6 kg. As shown in Fig. 3(a), the GSM−19T proton magnetometer, with an accuracy of ±0.2 nT, is carried by the multirotor UAV to conduct the aeromagnetic survey. The base station measuring mode is applied, and the GPS is used to synchronize the magnetometer and provide position data.

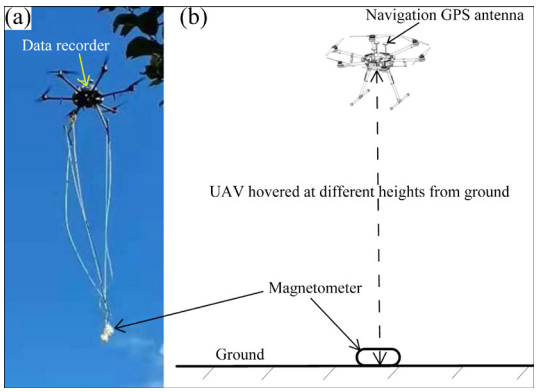

Fig. 3 Multirotor UAV system and diagram indicating process of measuring static interference: (a) Photograph of multirotor drone in study area; (b) Diagram of UAV interference test

Since materials with magnetism are used inside the UAV's fuselage, which cause the static interference on the measurement, it is necessary to measure the UAV's interference with the magnetic field beforehand. As shown in Fig. 3(b), the UAV is hovered at different heights from the ground to study its interference on the magnetometer. Intuitively, the larger the separation between the UAV and magnetometer is, the less the interference will be. In our tests, when the UAV hovered more than 5 m above the magnetometer, the interference was negligible to the measured magnetic data, as shown in Fig. 4(a). However, considering the fact that the magnetometer is suspended below the UAV by soft ropes, the distance between the magnetometer and the UAV should be shortened as much as possible, or flight dynamics and wind will easily affect their stability. One usual case is that the magnetometer will deviate from the UAV horizontally during the strong wind and further evolve into tow-swing movement around the UAV as the motors in the opposite direction increase the power output to maintain the position. This kind of tow-swing movement can impact the flight safety of the UAV.

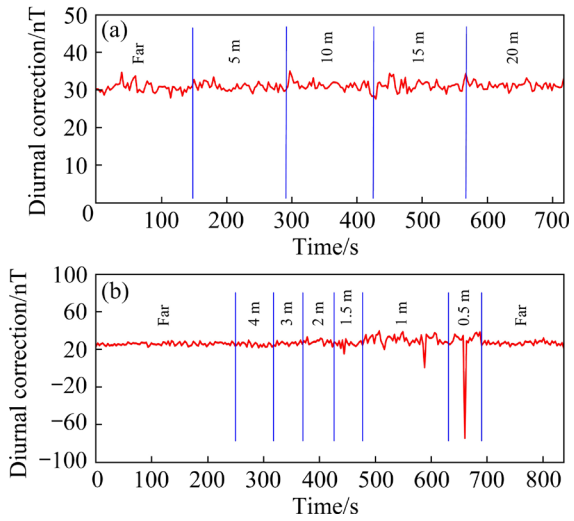

Fig. 4 Static interference investigation on diurnal correction with different separations between UAV and magnetometer: (a) With separation more than 5 m; (b) With separation less than 4 m

Significant interference occurs as the UAV is separated less than 2 m above the magnetometer as shown in Fig. 4(b). This interference includes both the static interference generated by the drone body and the dynamic interference generated by the motor. Multiple tests reveal that the positive anomaly (abnormality higher than the normal field) in the interference is relatively stable and is caused by the static interference of the fuselage, while the intensity of the negative anomaly (abnormality lower than the normal field) ascribed to the electrical current in the motor is random.

In order to investigate the random negative anomaly classified as dynamic interference that frequently occurs during strong wind, we compare the magnetic survey data of the UAV at different altitudes (above sea level). As the altitude rises and the wind increases, the UAV needs to increase its power output to maintain stability, which results in heavy dynamic interference. As shown in Fig. 5(a), when the fly altitude is less than 720 m, the measured data decreases smoothly with the altitude rising. The wind at a high altitude can result in heavy dynamic interference with values more than 1000 nT illustrated in Fig. 5(b).

Based on tests at various distances between the magnetometer and the UAV, magnetometer is held 3 m below the UAV in this experiment, considering the safety and factors of static interference. However, due to the dense vegetation and fog in the mountains, the visibility is low, the actual flight altitude of the UAV is more than 800 m, and the strong winds probably result in a noise greater than −1000 nT in the magnetic measurements.

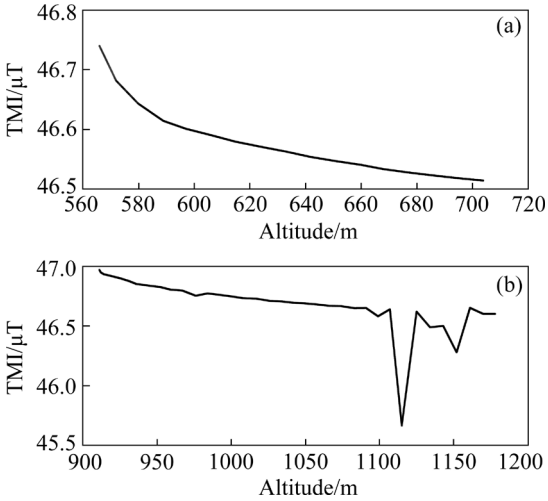

Fig. 5 Observational data at different altitudes (TMI: Test magnetic interference): (a) Magnetic survey data at lower altitudes; (b) Magnetic survey data at higher altitudes

3.2 Flight operations

This survey is performed on a high mountain with the lowest and highest altitudes of approximately 500 and 1450 m, respectively. The average slope of the mountain is about 40°, which results in difficulties for a ground survey. Since the flight-control signal cannot pass through the mountains, the study area is divided into several blocks according to the terrain conditions. This test has 16 landing pads noted by red triangles shown in Fig. 6(a), and each pad is used for flight only within

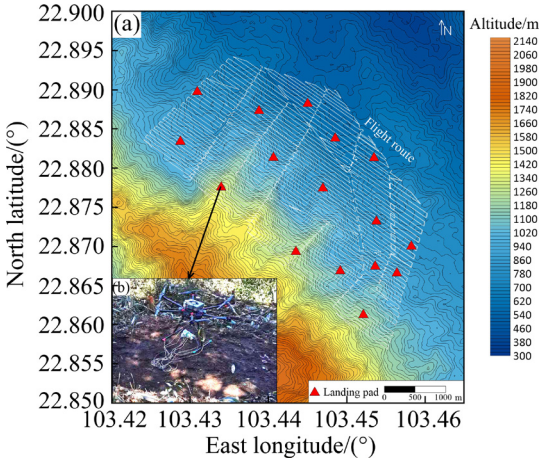

Fig. 6 Flight routes and landing pads: (a) Flight routes indicated by white line; (b) Photograph of landing pad

the visible area confined by surrounding mountains. As shown in Fig. 6(b), each landing pad requires approximately 10 m^2 ground clearance for the UAV, and it is generally set on the high ridges to have an unobstructed view of all flight routes within the operating area.

Altizure software is used to plan routes and complete flights automatically. The altitude of the flight is 120 m with the highest altitude of each survey block. The flight-line distance is 50 m, the azimuth is 145°, and the flight speed is 7 m/s. The power of the UAV is monitored in real-time, and the UAV will return when the power decreases to approximately 30%. The UAV completed about 100 flights and covered 7.8 km^2. Four accidents occurred, which consisted of three times during landing, and one hit a tree branch during a turn.

3.3 Noise reduction

To eliminate the strong interference caused by the motor and noise, the interference caused by wind and UAV needs to be identified firstly. After picking out the interference, the data with interference should be processed by replacing compromised observation with interpolation from the neighboring data points and applying a filter to get a smooth result. The detailed instructions are as follows.

(1) Determine the maximum value (T_{max}) and minimum value (T_{min}) of the normal magnetic field. Firstly, we calculate the standard deviation (σ) of the magnetic data [20]:

$$\sigma=\sqrt{\frac{\sum_{i=1}^{n}(t_i-\overline{t})^2}{n-1}} \tag{1}$$

where t_i is the data of each measuring point, $\overline{t}$ is the mean value of the entire raw data set, and n is the total number of magnetic measuring points. Due to the large difference between the interference and the data, after deleting the data exceeding $\pm\sigma$, we calculate the standard deviation and average value of this edited magnetic measurement data again, and derive the normal distribution density $f(t)$ as follows [20]:

$$f(t)=\frac{1}{\sigma\sqrt{2\pi}}\exp\left[-\frac{(t-\overline{t})^2}{2\sigma^2}\right] \tag{2}$$

Then, we estimate the data fit according to the normal distribution density and frequency. If the magnetic survey data approximately conform to the normal distribution, then there will exist

$$\begin{cases}T_{max}=\overline{t}+3\sigma\\ T_{min}=\overline{t}-3\sigma\end{cases} \tag{3}$$

(2) Delete bad data and interpolate the nearby observations to supplement the missing data. Delete the data beyond the range between T_{min} and T_{max}, and the replace the data by interpolation using inverse distance weighting method. The search radius of the interpolation is 4 times the route distance (200 m). The normal measuring point data within the search radius are used as neighboring points, and the interpolation is calculated as follows [21]:

$$Z_j=\sum_{i=1}^{n}\frac{Z_i}{d_{ij}{}^{\beta}}\Bigg/\sum_{i=1}^{n}\frac{1}{d_{ij}{}^{\beta}} \tag{4}$$

where Z_j is the interpolated value for point j, Z_i is the neighboring point, d_{ij} is the distance between point j and neighboring point of point i, and β is the weighting power, which is generally pre-set to be 2.

(3) Filter the data. The data in the range from T_{min} to T_{max} also have interference, which results in a large gap between some data and their neighboring data. To maintain the continuity of the data, a nonlinear filtering method of threshold averaging is adopt. The relative error (ε_i) of each measuring point within the range of the survey line distance is calculated as

$$\varepsilon_i=\left|\frac{T_i-\overline{T}}{\overline{T}}\right|\times100\% \tag{5}$$

where T_i is the point data, and $\overline{T}$ is the mean value within the range of the line distance. If ε_i exceeds a certain threshold, we use $\overline{T}$ instead of ε_i. The threshold used in this data processing is 70%.

In order to verify the denoising algorithm, we carried out the numerical experiment. There are 441 synthetic data points with data value T evenly distributed with 10 m spacing in an area of 200 m × 200 m. As shown in Fig. 7(a), the initial data points with the same y-coordinate have equal data values, and the data value increases with 0.2 nT/m along y-axis. The point located at (0, 0) m has the starting value of 200 nT. As shown in Fig. 7(b), there are 10 strong magnetic interferences randomly added to the synthetic data points, each with noise level of −1000 nT. The results of noise reduction by using the proposed algorithm are shown

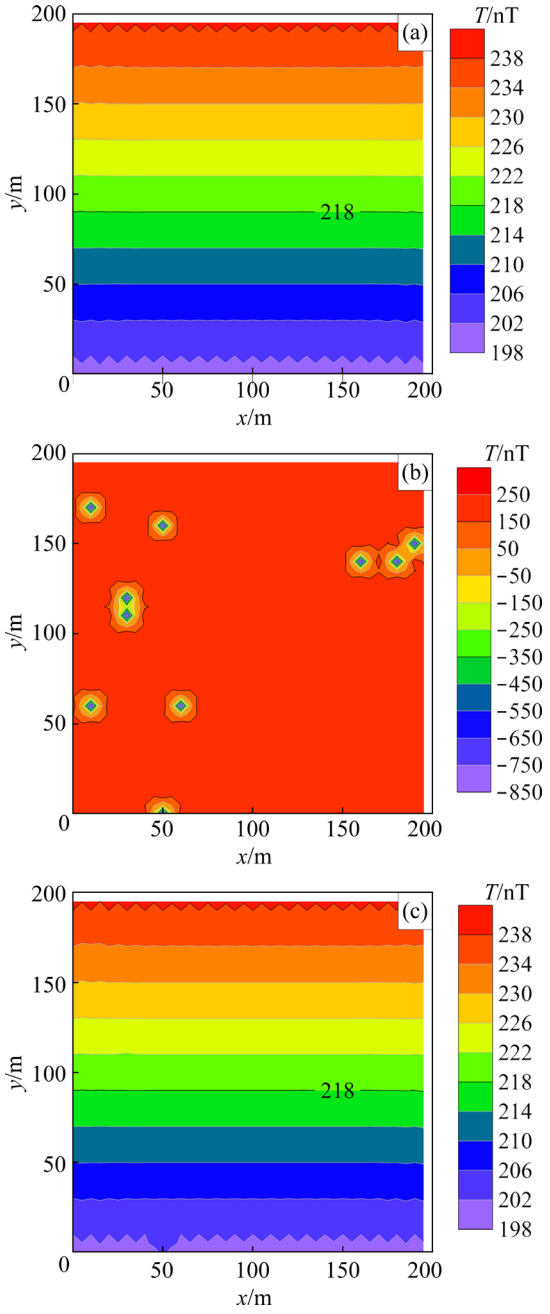

Fig. 7 Diagrams of noise reduction processing of synthetic model: (a) Initial data without noise; (b) Data with strong interference; (c) Data after denoising

in by Fig. 7(c). The data are recovered since these strong interferences are suppressed by the denoising algorithm.

Table 1 lists the details of the denoising algorithm on these 10 contaminated data points, the relative error is ±1.1%, and the total mean square relative error is ±0.37%. The numerical experiment demonstrates that the proposed denoising algorithm is able to suppress the strong magnetic interference effectively.

Table 1 Analysis of denoising effect

x/m	*y*/m	*T*/nT			Relative error/%
		Model data	Noisy data	Denoising data	
50	0	200.0	−800	202.2	1.10
30	110	222.0	−778	221.8	−0.08
30	120	224.0	−776	224.1	0.06
160	140	228.0	−772	228.0	−0.01
180	140	228.0	−772	227.9	−0.04
190	150	230.0	−770	230.1	0.05
50	160	232.0	−768	232.0	0.00
10	170	234.0	−766	233.8	−0.10
60	60	212.0	−788	212.0	0.00
10	60	212.0	−788	212.0	0.00
Mean square relative error/%					0.37

4 Results and discussion

After the magnetic measurement data of this survey are corrected by diurnal variation correction, horizontal gradient correction, and altitude correction, the mean value of all data is subtracted to obtain ΔT.

The calculated standard deviation of these magnetic measurement data is 1143 nT. Since the large deviation between the local noise data and the mean data, the data exceeding ±1143 nT are first eliminated, and then a normal distribution test is performed. These processes reduce the influence of abnormal data on the statistics of the normal distribution. As shown in Fig. 8, the data roughly conform to the characteristics of a normal distribution.

Figure 9(a) shows that the plane distribution of negative anomalies (abnormalities lower than the

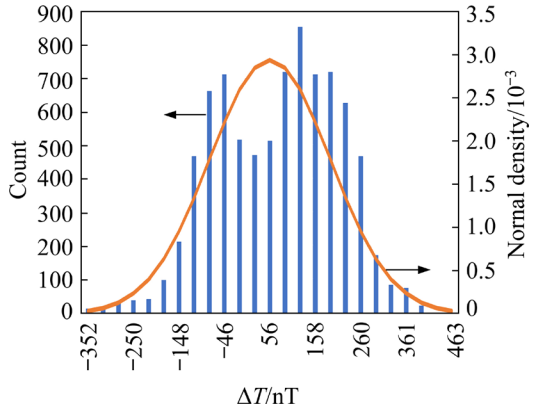

Fig. 8 Statistical graph of normal distribution of magnetic data

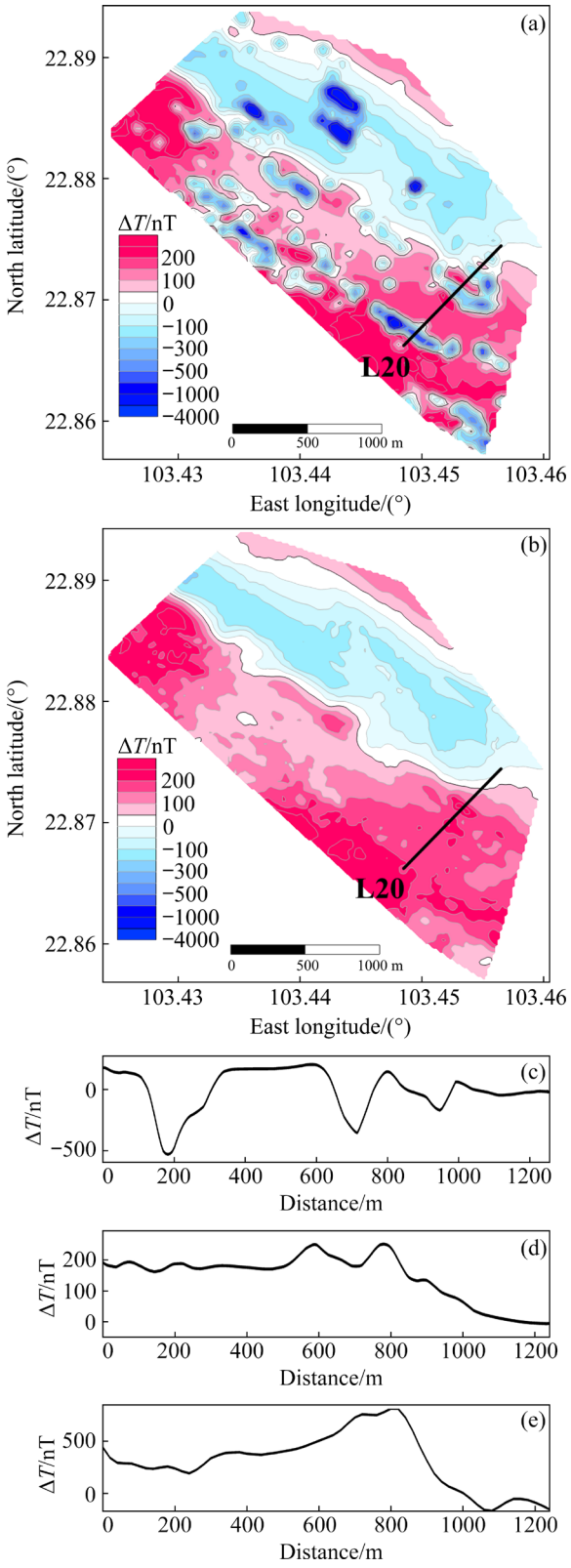

Fig. 9 Evaluation of denoising work for study area by aeromagnetic measurements: (a) Original data of aeromagnetic survey; (b) Data after noise processing; (c) Original data of L20 by aeromagnetic survey; (d) Denoised data of L20 by aeromagnetic survey; (e) Original data of L20 by ground magnetic survey

normal field) is consistent with the direction of the route. The negative anomalies are locally greater than −2000 nT, which is the noise data probably caused by the UAV motor under the influence of strong wind.

The calculated effective numerical range is from −352 to 463 nT. Data out of the range are interpolated by inverse distance weighting method. After filtering, the contour map is shown in Fig. 9(b)

The local negative anomaly with a large value is eliminated after the noise reduction process shown in Fig. 9(b). The positive and negative distribution of ΔT is clearer, and the regional distributional characteristics of the geomagnetic field are retained. As shown in Figs. 9(c), (d), and (e), the negative interference anomaly on the L20 profile is eliminated after the noise reduction process, and the positive and negative changes in the aeromagnetic data are basically consistent with the ground magnetic survey.

The basic magmatic rock containing titanomagnetite is the target geological body of this survey. The reduction to the pole (RTP) calculation of ΔT can transform the oblique magnetization into vertical magnetization, which requires the geomagnetic inclination and the geomagnetic declination of the titanomagnetite in the study area. The measured data of the directional specimens collected from the nearby mining area show that the magnetic declination is 40° and the magnetic dip angle is 45°. Then, the RTP of ΔT is carried out, and the RTP contour map is applied to delineating the horizontal distribution of basic magmatic rock.

As shown in Fig. 10(a), the western magnetic anomaly after RTP calculation agrees well with the exposed distribution of basic magmatic rocks. According to the magnetic anomaly of high value in the RTP contour map, the underground basic magmatic rock is linearly distributed along the NW−SE direction, and the magnetic anomaly in the middle of the survey area is caused by the extension of the known basic magmatic rock in the mining area to the southeast. Based on these deductions, four boreholes were drilled to verify the existence of concealed basic magmatic rocks. As shown in Figs. 10(b) and (c), these four boreholes reveal titanium magnetite bodies, which verify the value of the aeromagnetic survey in the study area.

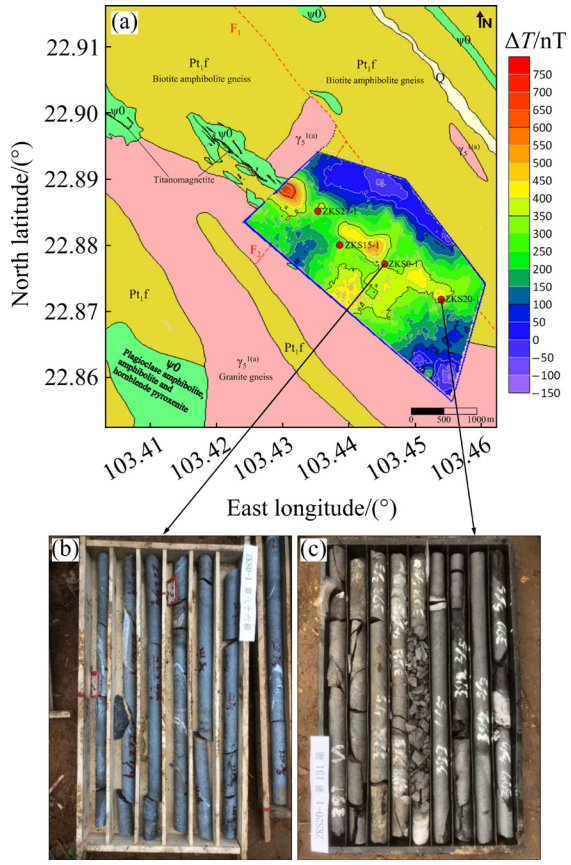

Fig. 10 Verification of aeromagnetic survey by geological map and cores extracted from boreholes: (a) Aeromagnetic RTP contour and geological map; (b) Titanium magnetite core drilled from ZKS0-1; (c) Titanium magnetite core drilled from ZKS20-1

According to the exposure of these boreholes (ZKS15-1, ZKS0-1, ZKS27-1 and ZKS20-1), the strike of the ore body is along NW−SE (130°−310°). This survey covers more than 2 km length of the ore body with dip of SW (45°−65°). We can also infer from the aeromagnetic RTP contour map and geological map that the ore body in the study area is the southeast extension of the ore body in the nearby mining area.

5 Conclusions

(1) A multirotor UAV equipped with a proton magnetometer was used to carry out aeromagnetic survey in Jinping (a mountainous area), Yunnan, China. The survey line was 156 km long, and the covered survey area was 7.8 km^2. The aeromagnetic test took only 10 d rather than about 50 d by the ground magnetic survey.

(2) The static interference was investigated by holding the proton magnetometer at different separations from the multirotor UAV, and 3 m was chosen for safety concerns. Since the dynamic interference due to the strong wind is random and heavily affects the magnetic data and flight safety, we proposed a denoising algorithm that mainly depends on noise identification and replacement by numerical statistics to suppress the dynamic noise multirotor UAV.

(3) The magnetic anomaly after RTP calculation based on denoised data shows that there are basic magmatic rocks connected with the mining area in the study area. It is verified that the basic magmatic rocks contain titanomagnetite by four drill boreholes at locations, which are inferred from aeromagnetic data.

Acknowledgments

This work was jointly supported by the National Natural Science Foundation of China (Nos. 42130810, 42004065, 42074165), and the Key Research and Development Program of Hunan Province, China (No. 2020SK2058).

References

[1] SALEM A, ALI M Y. Mapping basement structures in the northwestern offshore of Abu Dhabi from high-resolution aeromagnetic data [J]. Geophysical Prospecting, 2016, 64: 726−740.

[2] RAZAVI PASH R R, DAVOODI Z, MUKHERJEE S, DEHSARVI L H, GHASEMI-ROZVEH T G. Interpretation of aeromagnetic data to detect the deep-seated basement faults in fold thrust belts: NW part of the petroliferous Fars province, Zagros belt, Iran [J]. Marine and Petroleum Geology, 2021, 133: 105292.

[3] D'AMOUR U J, NGARUYE J C, SAIBI H. Defining potential mineral exploration targets from the interpretation of aeromagnetic data in western Rwanda [J]. Ore Geology Reviews, 2021, 128: 103927.

[4] AN S, ZHOU K F, WANG J L, ZHANG N N, LIAO S B, FENG Q W, ZHANG Z X. Interpretation of high resolution aeromagnetic data for structures study and exploration of polymetallic deposits in Kalatage area, eastern Tianshan (NW China) [J]. Geosciences Journal, 2020, 24: 315−327.

[5] GE T F, QIU L, HE J Z, FAN Z G, HUANG X Z, XIONG S Q. Aeromagnetic identification and modeling of mafic-ultramafic complexes in the Huangshan−Turaergen Ni−Cu metallogenic belt in NW China: Magmatic and metallogenic implications [J]. Ore Geology Reviews, 2020, 127: 103849.

[6] KOYAMA T, KANEKO T, OHMINATO T, YANAGISAWA T, TAKEO M. An aeromagnetic survey of Shinmoe-dake volcano, Kirishima, Japan, after the 2011 eruption using an unmanned autonomous helicopter [J]. Earth, Planets and

Space, 2013, 65(6): 657−666.
[7] WOOD A, COOK I, DOYLE B, CUNNINGHAM M, SAMSON C. Experimental aeromagnetic survey using an unmanned air system [J]. The Leading Edge, 2016, 35(3): 214−300.
[8] HASHIMOTO T, KOYAMA T, KANEKO T, OHMINATO T, YANAGISAWA T, YOSHIMOTO M, SUZUKI E. Aeromagnetic survey using an unmanned autonomous helicopter over Tarumae Volcano, northern Japan [J]. Exploration Geophysics, 2014, 45: 37−42.
[9] JIANG D D, ZENG Z F, ZHOU S, GUAN Y W, LIN T. Integration of an aeromagnetic measurement system based on an unmanned aerial vehicle platform and its application in the exploration of the Ma'anshan magnetite deposit [J]. IEEE Access, 2020, 8: 189576−189586.
[10] KIM B, LEE S, PARK G, CHO S J. Development of an unmanned airship for magnetic exploration [J]. Exploration Geophysics, 2021, 52(4): 462−467.
[11] MALEHMIR A, DYNESIUS L, PAULUSSON K, PAULUSSON A, JOHANSSON H, BASTANI M, WEDMARK M, MARSDEN P. The potential of rotary-wing UAV-based magnetic surveys for mineral exploration: A case study from central Sweden [J]. The Leading Edge, 2017, 36(7): 538−620.
[12] BIAN J, WANG X B, GAO S. Experimental aeromagnetic survey using a rotary-wing aircraft system: A case study in Heizhugou, Sichuan, China [J]. Journal of Applied Geophysics, 2021, 184: 104245.
[13] WU P L, ZHANG Q Y, CHEN L Z, FANG G Y. Analysis on systematic errors of aeromagnetic compensation caused by measurement uncertainties of three-axis magnetometers [J]. IEEE Sensors Journal, 2019, 19(1): 361−369.
[14] MU Y X, ZHANG X J, XIE W P, ZHENG Y X. Automatic detection of near-surface targets for unmanned aerial vehicle (UAV) magnetic survey [J]. Remote Sensing, 2020, 12: 452.
[15] CUNNINGHAM M, SAMSON C, WOOD A, COOK I. Aeromagnetic surveying with a rotary-wing unmanned aircraft system: A case study from a zinc deposit in nash creek, New Brunswick, Canada [J]. Pure and Applied Geophysics, 2018, 175: 3145−3158.
[16] PEI Y L, LIU B H, LIU C G, JI Y Q. An aeromagnetic survey system based on an unmanned autonomous helicopter: Development, experiment, and analysis [J]. International Journal of Remote Sensing, 2017, 38(8/9/10): 3068−3083.
[17] LIU H, DONG H B, GE J, LIU Z, YUAN Z W, ZHU J, ZHANG H Y. Efficient performance optimization for the magnetic data readout from a proton precession magnetometer with low-rank constraint [J]. IEEE Transactions on Magnetics, 2019, 55(8): 1−4.
[18] GE J, LI H, LUO W, DONG H, LIU H, WANG H, WANG W, YUAN Z, ZHU J, ZHANG H. Aeromagnetic system for a Multi-rotor unmanned aerial vehicle based on the Overhauser sensor [J]. Journal of Instrumentation, 2019, 14: P01015.
[19] QIAO Z, ZHOU S, JIAO J, YU P, ZHANG Z, ZHOU W, WU G. Research on aeromagnetic three-component error compensation technology for multi-rotor UAV [J]. Journal of Applied Geophysics, 2021, 193: 104406.
[20] LOEVE M. Probability theory [M]. New York: Nostrand Company, Inc., 1955.
[21] LIU Z, ZHANG Z L, ZHOU C Y, MING W H, DU Z C. An adaptive Inverse-distance weighting interpolation method considering spatial differentiation in 3D geological modeling [J]. Geosciences, 2021, 11(2): 51.

多旋翼无人机航磁在中国云南省金平地区找矿中的应用

柳建新[1,2]，刘慧鹏[1,3]，刘 嵘[1,2]，薛建强[1,2]，李粤华[4]，王 芳[3]

1. 中南大学 地球物理与信息学院，长沙 410083；
2. 中南大学 有色资源与地质灾害探查湖南省重点实验室，长沙 410083；
3. 中国有色金属工业昆明勘察设计研究院有限公司 云南省岩土工程与地质灾害重点实验室，昆明 650051；
4. Climate Change Research Center, University of New South Wales, Sydney NSW 2052, Australia

摘 要：为了对中国云南省金平县地区隐伏磁铁矿体进行探测，使用多旋翼无人机对 7.8 km^2 的目标区域进行航磁测量，克服了该地区高海拔、地形崎岖、植被茂密等带来的地面勘查困难。通过现场试验对观测噪声来源与噪声水平进行研究。然后，将质子磁力仪置于距离多旋翼无人机下方 3 m 处位置以减小静态噪声。提出非线性滤波与逆距离加权插值算法以抑制由强风导致的动态噪声。结果表明，这些方法能减缓无人机旋翼和强风的干扰，经过处理的实测航磁数据与已知地层的水平分布吻合良好。根据航磁测量结果，在布置的 4 口钻井中都勘测到了隐伏的钛磁铁矿，证明旋翼无人机航磁测量找矿的有效性。

关键词：航空磁测；多旋翼无人机；噪声抑制；隐伏钛磁铁矿

(Edited by Wei-ping CHEN)